Title

A variable resolution approach for improved acquisition of hyperpolarized 13C metabolic MRI

Journal

Magnetic Resonance in Medicine, 84(6)

ISSN

0740-3194

Authors

Gordon, Jeremy W
Autry, Adam W
Tang, Shuyu
et al.

Publication Date

2020-12-01

DOI

10.1002/mrm.28421

Peer reviewed

HHS Public Access

Author manuscript

Magn Reson Med. Author manuscript; available in PMC 2020 December 07.

Published in final edited form as:

Magn Reson Med. 2020 December ; 84(6): 2943–2952. doi:10.1002/mrm.28421.

A variable resolution approach for improved acquisition of hyperpolarized ^{13}C metabolic MRI

Jeremy W. Gordon[1], **Adam W. Autry**[1], **Shuyu Tang**[1,2], **Jasmine Y. Graham**[1,2], **Robert A. Bok**[1], **Xucheng Zhu**[1,2], **Javier E. Villanueva-Meyer**[1], **Yan Li**[1], **Michael A. Ohilger**[1], **Maria Roselle Abraham**[3], **Duan Xu**[1,2], **Daniel B. Vigneron**[1,2], **Peder E. Z. Larson**[1,2]

[1]Department of Radiology and Biomedical Imaging, University of California San Francisco, San Francisco, California, USA

[2]UC Berkeley-UCSF Graduate Program in Bioengineering, University of California San Francisco and University of California, Berkeley, California, USA

[3]Division of Cardiology, Department of Medicine, University of California San Francisco, San Francisco, California, USA

Abstract

Purpose: To ameliorate tradeoffs between a fixed spatial resolution and signal-to-noise ratio (SNR) for hyperpolarized ^{13}C MRI.

Methods: In MRI, SNR is proportional to voxel volume but retrospective downsampling or voxel averaging only improves SNR by the square root of voxel size. This can be exploited with a metabolite-selective imaging approach that independently encodes each compound, yielding high-resolution images for the injected substrate and coarser resolution images for downstream metabolites, while maintaining adequate SNR for each. To assess the efficacy of this approach, hyperpolarized [1-^{13}C]pyruvate data were acquired in healthy Sprague-Dawley rats ($n = 4$) and in two healthy human subjects.

Results: Compared with a constant resolution acquisition, variable-resolution data sets showed improved detectability of metabolites in pre-clinical renal studies with a 3.5-fold, 8.7-fold, and 6.0-fold increase in SNR for lactate, alanine, and bicarbonate data, respectively. Variable-resolution data sets from healthy human subjects showed cardiac structure and neuro-vasculature in the higher resolution pyruvate images (6.0×6.0 mm^2 for cardiac and 7.5×7.5 mm^2 for brain) that would otherwise be missed due to partial-volume effects and illustrates the level of detail that can be achieved with hyperpolarized substrates in a clinical setting.

Conclusion: We developed a variable-resolution strategy for hyperpolarized ^{13}C MRI using metabolite-selective imaging and demonstrated that it mitigates tradeoffs between a fixed spatial resolution and SNR for hyperpolarized substrates, providing both high resolution pyruvate and coarse resolution metabolite data sets in a single exam. This technique shows promise to improve

Correspondence: Jeremy W. Gordon, Department of Radiology and Biomedical Imaging, University of California San Francisco, 1700 4th St, Byers Hall 102, San Francisco, CA 94158, USA. jeremy.gordon@ucsf.edu.

SUPPORTING INFORMATION

Additional Supporting Information may be found online in the Supporting Information section.

future studies by maximizing metabolite SNR while minimizing partial-volume effects from the injected substrate.

Keywords

carbon-13; EPI; hyperpolarization; MRI; pyruvate

1 | INTRODUCTION

Hyperpolarization (HP) via dissolution dynamic nuclear polarization[1] overcomes the poor receptivity of ^{13}C nuclei at clinical field strengths by providing a four to five orders of magnitude increase in signal, enabling dynamic imaging of both the injected substrate and downstream metabolites. Metabolic imaging with hyperpolarized substrates has been used to non-invasively image metabolism in cancer[2] and diabetes,[3] as well as neuroinflammatory disorders[4] and liver[5] and heart disease.[6] It has also shown the potential to both stage disease[7,8] and assess treatment response.[9]

Even with a 50,000-fold increase in polarization, SNR is often a limiting factor when imaging metabolic products, such as ^{13}C bicarbonate from [1-^{13}C]pyruvate, or TCA metabolites from [2-^{13}C]pyruvate, due to low concentrations, slow transport across the cell membrane, limited rates of conversion, and short T_1 relaxation times. This results in a 10 to 100-fold difference in signal-to-noise ratio (SNR) between HP ^{13}C-pyruvate and its metabolites,[10] yielding a mismatch in the supported spatial resolution[11] and a tradeoff between finer spatial resolution and detectability of metabolic products. Obtaining high resolution pyruvate data is especially important to separate the hyperpolarized substrate signal in the vasculature and to minimize partial-volume effects that can confound quantification of cellular metabolism,[12–14] but this finer resolution limits detection of metabolites with lower SNR. While flow suppression techniques for hyperpolarized applications[13–16] can remove signal from fast flowing vascular spins at coarse resolutions, they also eliminate valuable modeling information that can be obtained from the vascular input function.[17]

One unique feature of MR among imaging modalities is the relationship between SNR and voxel size. Unlike other imaging modalities, the SNR in MRI is proportional to voxel volume, but retrospective downsampling or voxel averaging after acquisition only improves SNR by the square root of the voxel size.[18] Given that the readout duration remains the same, there is, therefore, an SNR benefit to acquiring data at a coarse resolution rather than retrospectively downsampling high resolution data after acquisition. While this cannot be readily exploited with chemical shift imaging since spectral and spatial information is simultaneously encoded for all metabolites, metabolite-selective imaging methods for HP ^{13}C using echoplanar,[19,20] spiral,[21] or Cartesian[22,23] trajectories encode each metabolite independently. This independent acquisition strategy has been previously exploited with variable flip angle approaches[24–26] to improve signal from downstream metabolites while reducing radiofrequency (RF)-induced signal loss from the injected substrate. It would also, in principle, enable a variable resolution approach to tailor the spatial resolution to each metabolite.

To explore the potential of acquiring variable-resolution data, in this work we used a metabolite-selective imaging approach to independently excite [1-^{13}C]pyruvate and downstream metabolites. In this approach, a single-band spectral-spatial (SPSP) RF pulse was used to selectively excite each metabolite followed by a single-shot readout to rapidly encode the magnetization. The spatial resolution was tailored for each metabolic product by independently scaling the encoding gradients, yielding high-resolution images for pyruvate and coarser resolution for downstream metabolites, while maintaining adequate SNR for each.

2 | METHODS

All studies were performed on a 3T MR scanner (MR750, GE Healthcare) with a gradient performance of 50 mT/m maximum gradient strength and 200 T/m/s maximum slew-rate. The single-band SPSP RF pulses were designed using the SPSP RF toolbox, which can be accessed at https://github.com/LarsonLab/hyperpolarized-mri-toolbox/.[27]

2.1 | Pre-clinical studies

To assess the efficacy of this approach, two HP [1-^{13}C]pyruvate injections were performed in healthy Sprague Dawley rats (n = 4), separated in time by at least 55 min. All animal studies were conducted under protocols approved by the University of California San Francisco Institutional Animal Care and Use Committee (IACUC). Rats were anesthetized with ~1.5% isoflurane delivered via oxygen gas at 1 L/min and placed on a heated pad throughout the duration of the experiment. Aliquots containing 24 μL [1-^{13}C] pyruvic acid doped with 15 mM trityl radical (Ox063, GE Healthcare) and 1 mM Gd-DOTA were polarized in a HyperSense system (Oxford Instruments, Abingdon UK) operating at 1.35 K and 3.35 T. After 1 h, samples were rapidly dissolved and neutralized with 4 mL of superheated water containing 80 mM NaOH, 40 mM Tris buffer, and 0.3 mM ethylenediaminetetraacetic acid (EDTA). Following rapid dissolution and neutralization, ~2.6 mL pyruvate was injected over 12 s via tail vein cannulation. Imaging began when the injection started.

Hyperpolarized ^{13}C data were acquired with a metabolite-selective imaging approach, using a single-band SPSP RF pulse for excitation (passband full-width half-maximum [FWHM] = 130 Hz, stopband = 868 Hz) and a single-shot symmetric echoplanar readout for encoding.[28] Scan parameters were 250 ms repetition time (TR), 24.1 ms echo time (TE), 32 × 24 matrix size (75% partial-Fourier), 1.27 ms echo spacing, 20 total timepoints. A 2 s delay was added to yield a temporal resolution of 3 s and a total scan time of 60 s. A single slice was centered on the kidneys with a slice thickness of 15–20 mm, chosen to be large enough to completely cover one kidney. Pyruvate was excited with a 10° flip angle while the metabolites lactate, alanine, and bicarbonate received a 30° flip angle.

HP MR data from the first injection were acquired with a constant 2.5 × 2.5 mm^2 in-plane resolution (field of view [FOV] = 8.0 × 8.0 cm^2), while data from the second injection were acquired with the variable resolution approach. Here, pyruvate was acquired at 2.5 × 2.5 mm^2, lactate at 5.0 × 5.0 mm^2, and alanine and bicarbonate at 7.5 × 7.5 mm^2 by varying the FOV. Since each metabolite was acquired independently, this was readily accomplished by

reducing G_x and G_y to increase the voxel size, while maintaining the same readout duration and matrix size (Figure 1). All other scan parameters were identical for both injections.

2.2 | Human studies in healthy volunteers

Brain and cardiac studies were performed in two healthy human volunteer subjects following Institutional Review Board- and Food and Drug Administration Investigational New Drug-approved protocols with informed consent. Samples containing 1.47 g of Good Manufacturing Practice (GMP) grade [1-^{13}C]pyruvic acid (MilliporeSigma Isotec) and 15 mM electron paramagnetic agent (EPA; AH111501, GE Healthcare) were prepared by a pharmacist the morning of the study and polarized using a SPINlab polarizer (GE Healthcare) operating at 5 T and 0.8 K for 3 h. Following dissolution, the EPA was removed by filtration, the solution neutralized with a TRIS-buffered NaOH solution, and the quality control (QC) parameters of pH, pyruvate and residual EPA concentrations, polarization, and temperature were measured prior to injection. In parallel, the integrity of the 0.2 μm sterile filter was tested in agreement with manufacturer specifications prior to injection. After release by the pharmacist, a 0.43 mL/kg dose of ~250 mM pyruvate was injected at a rate of 5 mL/s, followed by a 20 mL sterile saline flush (0.9% sodium chloride, Baxter Healthcare Corporation).

One hyperpolarized ^{13}C brain data set was acquired with the EPI sequence described above using a birdcage coil for RF transmit with an integrated 24 element receiver (Rapid Biomedical, Würzburg, Germany). Scan parameters were 125 ms TR, 30.7 ms TE, 32 × 32 matrix size, ±19.23 kHz bandwidth (BW), 1.064 ms echo-spacing, eight 1.5-cm slices with an axial orientation. Data acquisition started 5 s after the end of saline injection. Pyruvate was excited with a 20° flip angle and acquired at 7.5 × 7.5 mm^2 resolution, while the metabolites lactate and bicarbonate received a 30° flip angle and were acquired at 15 × 15 mm^2 in-plane resolution. Twenty timeframes were acquired with a 3 s temporal resolution, yielding a total scan time of 1 min. Immediately following imaging, a non-localized spectrum was acquired for QC to confirm the center frequency was set correctly. For anatomic reference, a ^{1}H 3D inversion recovery spoiled gradient recalled (IR-SPGR) data set was acquired with the body coil. Scan parameters were 6.7 ms TR, 2.5 ms TE, 450 ms IR time, 25.6 × 25.6 × 18.6 cm^2 FOV, 256 × 256 × 124 matrix (1 × 1 × 1.5 mm^3 resolution).

One hyperpolarized ^{13}C cardiac data set was acquired with a metabolite-selective imaging approach, using the aforementioned single-band SPSP RF pulse and a single-shot spiral readout for encoding. Short-axis, cardiac gated data were acquired using a clamshell coil for RF transmit and an eight-channel paddle coil (4 × 2 array) for reception. Integrated bolus tracking, center frequency calibration, and B_1^+ calibration were performed using RT-Hawk[29] (HeartVista, Los Altos, CA). Scan parameters were 53 ms TR, 12.6 ms TE, 22 ms readout duration, five 2.1-cm thick slices, 30 timeframes. Pyruvate was excited with a 20° flip angle and acquired at 6 × 6 mm^2 in-plane resolution, while lactate and bicarbonate were excited with a 30° flip angle and acquired at 12 × 12 mm^2 in-plane resolution. Five slices (one metabolite volume) were acquired per cardiac trigger, yielding a temporal resolution of ~3.5 s and a total scan time of 105 s. For anatomic reference, a spoiled gradient echo (GRE) was

acquired using the ^{1}H body coil. Scan parameters were 12.8 ms TR, 2.78 ms TE, 48 × 48 cm^2 FOV, 160 × 160 matrix, 16 slices, 6 mm slice thickness.

2.3 | Reconstruction and analysis

Spiral data were reconstructed using a Kaiser-Bessel gridding method,[30] while EPI data were reconstructed using the Orchestra toolbox (GE Healthcare). For pre-clinical studies, EPI data were phase corrected and then interpolated to a Cartesian grid before partial-Fourier reconstruction. For the healthy volunteer EPI brain study, data were phase corrected and then Fourier transformed. For both healthy volunteer data sets, multichannel data were pre-whitened[31] and then coil combined using pyruvate to estimate the coil weights.[32]

For analysis, the peak dynamic SNR and area under the curve (AUC) ratio were determined for each metabolite. Peak dynamic SNR was calculated as the maximum voxel signal from each metabolite timecourse divided by the standard deviation of the noise, which was obtained from a timeframe and slice where no signal was present. The AUC ratio was defined as the total metabolite signal divided by the total pyruvate signal. The AUC for each metabolite was calculated by temporally summing the data and then taking the mean of the ROI signal. The raw signal in the variable resolution data sets was normalized to the voxel volume to allow for quantification between the variable-resolution data sets. Statistical significance was assessed with a paired *t*-test.

3 | RESULTS

The metabolite dynamics from the constant resolution rat kidney acquisition at 2.5 × 2.5 mm^2 can be seen in Figure 2, illustrating a clear mismatch in SNR between pyruvate and lactate, alanine, and bicarbonate. While pyruvate delivery and perfusion throughout the kidneys was clearly visible with high SNR, bicarbonate was not clearly observable at this spatial resolution. Here, downsampling the bicarbonate data to an effective resolution of 7.5 × 7.5 mm^2 (Supporting Information Figure S1B, which is available online) improves SNR and brings bicarbonate above the noise floor (SNR > 4) for three timeframes. Conversely, acquiring the bicarbonate data at 7.5 × 7.5 mm^2 using a variable resolution approach (Supporting Information Figure S1C) showed substantially improved conspicuity and further SNR improvement, with nine timeframes above an SNR = 4 threshold. The urea phantom is visible in the bicarbonate images because it is partially excited by the passband of the SPSP RF pulse (~70 Hz separation between urea and bicarbonate at 3T). The physical location of the urea phantom appears to be different because the voxel size was three-fold larger for the variable resolution bicarbonate acquisition, resulting in a three-fold larger chemical shift.

This improvement in SNR when acquiring data at a coarser resolution holds for both lactate (5.0 × 5.0 mm^2) and alanine (7.5 × 7.5 mm^2) as well. Tailoring the spatial resolution for each metabolite results in improved SNR throughout the entire timecourse (Figure 2). Peak dynamic SNR and AUC ratios are summarized in Table 1. The SNR was significantly improved ($P < .05$) for each of the variable resolution metabolites, with a 3.5-fold, 8.7-fold, and 6.0-fold increase in SNR for lactate, alanine, and bicarbonate data, respectively. The expected SNR improvements based on voxel volume changes were four-fold, nine-fold, and nine-fold for lactate, alanine, and bicarbonate, respectively. The less than expected

improvement in bicarbonate SNR was likely due to the undetectable signal in the constant resolution experiment, with the noise floor limiting the measured SNR gain. There was also a significant difference in the bicarbonate-to-pyruvate ratio between the constant and variable resolution experiments ($P < .05$). This is due to the noise detection limit improvement in the variable resolution experiment, as the bicarbonate in the constant resolution experiment was indistinguishable from noise (no significant difference between the constant resolution bicarbonate-to-pyruvate or noise-to-pyruvate ratios).

The dynamic timecourse and AUC results from the brain exam can be seen in Figures 3–4 and in Supporting Information Figures S2–S3. The high-resolution pyruvate data acquired at 7.5 × 7.5 mm^2 clearly depicts the vasculature, showing strong signal and improved delineation of both the arteries (proximal anterior cerebral circulation) and veins (superior sagittal, transverse, and sigmoid sinuses). Lactate and bicarbonate acquired at a coarser 15 × 15 mm^2 resolution show differential metabolism between the gray and white matter, with higher signal seen in the posterior fossa and gray matter structures. Peak dynamic SNR in this variable-resolution experiment was 288.8 for pyruvate, 14.8 for lactate, and 6.3 for bicarbonate. This approach gave sufficient SNR for each metabolite, providing both higher resolution pyruvate and coarser resolution lactate and bicarbonate data sets in a single exam. A variable-resolution acquisition is key to this approach, as lactate and bicarbonate (peak SNR of 14.8 and 6.3, respectively) would be near or below the noise floor if acquired at the higher 7.5 × 7.5 mm^2 resolution.

The dynamic timecourse and AUC results from the cardiac exam are displayed in Figures 5–6 and in Supporting Information Figures S4–S5. The pyruvate data acquired at 6.0 × 6.0 mm^2 have high SNR in the left and right ventricles (peak SNR = 1208) throughout the timecourse, with strong contrast and clear signal reduction seen between the ventricles and the myocardium. The papillary muscles were also clearly observable at this higher resolution. At the coarser 12.0 × 12.0 mm^2 resolution, strong signal was visible from lactate (peak SNR = 50.3) and bicarbonate (peak SNR = 13.4), with bicarbonate signal localized to the myocardium and lactate signal in both the myocardium and blood pool.

4 | DISCUSSION

In this work, we developed and investigated a variable resolution approach using metabolite-selective imaging with echoplanar and spiral readouts and demonstrated that it mitigates the tradeoffs between a fixed spatial resolution and SNR for hyperpolarized substrates and downstream metabolic products. In pre-clinical studies, this method enabled visualization of bicarbonate metabolism that would otherwise have been below the noise floor at the higher spatial resolution designed for pyruvate. In two healthy volunteer studies, this approach was used to acquire pyruvate data at higher spatial resolution (6.0 × 6.0 mm^2 for cardiac and 7.5 × 7.5 mm^2 for brain), a substantial improvement over prior brain data nominally acquired at 12 × 12 mm^2 Ref. 33 or 15 × 15 mm^2 Refs. 28,34 and prior cardiac data acquired at 8.8 × 8.8 mm^2.[6] This higher resolution enabled unambiguous visualization of cardiac structure and neurovascular features that would otherwise be obfuscated by partial-volume effects if acquired at a coarser resolution and is better suited for comparison and correlation to ^1H perfusion metrics.

The same readout gradient waveform and BW were used in the variable resolution studies, with the resolution change accomplished by reducing the encoding gradient strength to increase the FOV. Each metabolite map, therefore, had the same echo-time and echo-spacing/phase accumulation, resulting in identical noise characteristics and sensitivity to off-resonance artifacts. This also obviates any additional quantification concerns arising from potential T_2^* differences between metabolites. Signal from the variable-resolution data sets were normalized to their respective voxel volume for quantification. Quantification was not impacted, as the lactate-to-pyruvate and alanine-to-pyruvate AUC ratios in the pre-clinical studies were not significantly different between the constant and variable-resolution data sets ($P = .33$ and $P = .24$, respectively). Although the acquisition order was not randomized, repeat injections of pyruvate were not expected to influence the AUC ratio given the more than 55-min interval between experiments.[35] Prolonged exposure to isoflurane anesthesia at different doses has also been shown to have no observable effect on pyruvate metabolism in the kidneys or liver.[36] Nevertheless, care must be taken when using the variable-resolution approach. An improvement in SNR only occurs if there is signal throughout the voxel, so choosing too coarse of a voxel size would provide less than expected SNR gain and will result in partial-volume effects, leading to underestimation of metabolism. In this case, partial volume correction strategies like those used in PET-MR[37,38] or super resolution approaches[39,40] could be employed to ameliorate these effects. In particular, the higher spatial resolution pyruvate image could be used to constrain the reconstruction for the coarser resolution metabolites, similar in concept to prior ^{1}H diffusion work that combined data acquired at high and low spatial resolution to better estimate the crossing fibers and diffusion parameters.[41]

Variable resolution acquisitions in healthy human subjects showed cardiac structure and neuro-vasculature in the pyruvate data set that would otherwise be missed due to partial-volume effects and illustrates the level of detail that can be achieved with hyperpolarized substrates in a clinical setting, approaching that of ^{1}H MRSI and some positron emission tomography (PET) radiotracers.[42–45] A variable resolution approach would also be beneficial when the biodistribution of metabolites is the primary interest[34] or when performing co-polarization studies with inert perfusion agents, such as ^{13}C urea,[46] and would provide an opportunity to acquire high-resolution perfusion data for the vascular input function along with metabolic data in a single integrated acquisition. It may also have application in the study of other hyperpolarized nuclei, such as ^{129}Xe, where the gaseous phase magnetization is roughly 100 times higher than the dissolved phase magnetization.[47]

However, increasing the matrix size to accommodate higher spatial resolution places greater demands on shimming and B_0 homogeneity. Signal dropout in the posterior myocardium, most evident in the bicarbonate images, is caused by susceptibility-induced B_0 inhomogeneity arising from cardiac veins[48] and the lung-heart interface,[49] along with both the positioning and sensitivity falloff of the eight-channel paddle coil used in the cardiac volunteer study. This highlights the importance of shimming in these studies and the need to either use a shorter readout duration or incorporate a B_0 map into the reconstruction. Moreover, some geometric distortion was seen in the variable-resolution brain study due to the longer echo train length and readout duration, reducing the BW in the blip dimension.

This can be overcome with a multi-shot approach (at the cost of an increase in scan time) or by using either a dual-echo[50] or an alternating blipped acquisition[51] to account and correct for distortion.

5 | CONCLUSIONS

A variable resolution approach to metabolic imaging can ameliorate tradeoffs between spatial resolution and SNR that limit MRI of hyperpolarized ^{13}C substrates. This technique enables both higher resolution for the injected substrate as well as quantification at a coarser resolution for the lower SNR metabolites, such as bicarbonate, which would be undetectable at the higher resolution. This could improve future pre-clinical and clinical studies by maximizing metabolite SNR and allow for metabolism quantification while minimizing partial volume effects from the injected substrate.

Supplementary Material

Refer to Web version on PubMed Central for supplementary material.

ACKNOWLEDGMENTS

This work was supported by NIH grants U01EB026412, R01EB016741, P01CA118816, R01CA183071, and P41EB013598; a Myokardia Inc. Myoseeds award; the UCSF Resource Allocation Program; and an American Cancer Society Research Scholar Grant #131715-RSG-18-005-01-CCE.

Funding information

NIH, Grant/Award Number: P01CA118816, P41EB013598, R01CA183071, R01EB016741 and U01EB026412; American Cancer Society, Grant/Award Number: 131715-RSG-18-005-01-CCE

REFERENCES

1. Ardenkjær-Larsen JH, Fridlund B, Gram A, et al. Increase in signal-to-noise ratio of >10,000 times in liquid-state NMR. Proc Natl Acad Sci USA. 2003;100:10158–10163. [PubMed: 12930897]
2. Nelson SJ, Kurhanewicz J, Vigneron DB, et al. Metabolic imaging of patients with prostate cancer using hyperpolarized [1–13C]pyruvate. Sci Transl Med. 2013;5:198ra108.
3. Keshari KR, Wilson DM, Sai V, et al. Non-invasive in vivo imaging of diabetes-induced renal oxidative stress and response to therapy using hyperpolarized 13C dehydroascorbate magnetic resonance. Diabetes. 2015;64:344–352. [PubMed: 25187363]
4. Guglielmetti C, Najac C, Didonna A, Van der Linden A, Ronen SM, Chaumeil MM. Hyperpolarized 13C MR metabolic imaging can detect neuroinflammation in vivo in a multiple sclerosis murine model. Proc Natl Acad Sci. 2017;114:E6982–E6991. [PubMed: 28760957]
5. Moon C-M, Shin S-S, Lim N-Y, et al. Metabolic alterations in a rat model of hepatic ischaemia reperfusion injury: In vivo hyperpolarized 13C MRS and metabolic imaging. Liver Int. 2018;38:1117–1127. [PubMed: 29345050]
6. Cunningham CH, Lau JY, Chen AP, et al. Hyperpolarized 13C metabolic MRI of the human heart: Initial experience. Circ Res. 2016;119:1177–1182. [PubMed: 27635086]
7. Granlund KL, Tee S-S, Vargas HA, et al. Hyperpolarized MRI of human prostate cancer reveals increased lactate with tumor grade driven by monocarboxylate transporter 1. Cell Metab. 2019;31:105–114.e3. [PubMed: 31564440]
8. Albers MJ, Bok R, Chen AP, et al. Hyperpolarized 13C lactate, pyruvate, and alanine: Noninvasive biomarkers for prostate cancer detection and grading. Cancer Res. 2008;68:8607–8615. [PubMed: 18922937]

9. Aggarwal R, Vigneron DB, Kurhanewicz J. Hyperpolarized 1-[13C]-pyruvate magnetic resonance imaging detects an early metabolic response to androgen ablation therapy in prostate cancer. Eur Urol. 2017;72:1028–1029. [PubMed: 28765011]
10. Park JM, Josan S, Jang T, et al. Volumetric spiral chemical shift imaging of hyperpolarized [2–13c]pyruvate in a rat c6 glioma model. Magn Reson Med. 2015;75:973–984. [PubMed: 25946547]
11. Wilson DM, Keshari KR, Larson PEZ, et al. Multi-compound polarization by DNP allows simultaneous assessment of multiple enzymatic activities in vivo. J Magn Reson. 2010;205:141–147. [PubMed: 20478721]
12. Lee H, Lee J, Joe E, et al. Flow-suppressed hyperpolarized 13C chemical shift imaging using velocity-optimized bipolar gradient in mouse liver tumors at 9.4 T. Magn Reson Med. 2017;78:1674–1682. [PubMed: 28019020]
13. Gordon JW, Niles DJ, Adamson EB, Johnson KM, Fain SB. Application of flow sensitive gradients for improved measures of metabolism using hyperpolarized 13c MRI. Magn Reson Med. 2015;75:1242–1248. [PubMed: 25951611]
14. Lau AZ, Miller JJ, Robson MD, Tyler DJ. Cardiac perfusion imaging using hyperpolarized 13c urea using flow sensitizing gradients. Magn Reson Med. 2016;75:1474–1483. [PubMed: 25991580]
15. Larson PEZ, Kerr AB, Reed GD, et al. Generating super stimulated-echoes in MRI and their application to hyperpolarized C-13 diffusion metabolic imaging. IEEE Trans Med Imaging. 2012;31:265–275. [PubMed: 22027366]
16. Fuetterer M, Busch J, Peereboom SM, et al. Hyperpolarized 13C urea myocardial first-pass perfusion imaging using velocity-selective excitation. J Cardiovasc Magn Reson. 2017;19:46. [PubMed: 28637508]
17. Sun C-y Walker CM, Michel KA Venkatesan AM, Lai SY Bankson JA. Influence of parameter accuracy on pharmacokinetic analysis of hyperpolarized pyruvate. Magn Reson Med. 2018;79:3239–3248. [PubMed: 29090487]
18. Edelstein WA, Glover GH, Hardy CJ, Redington RW. The intrinsic signal-to-noise ratio in NMR imaging. Magn Reson Med. 1986;3:604–618. [PubMed: 3747821]
19. Cunningham CH, Chen AP, Lustig M, et al. Pulse sequence for dynamic volumetric imaging of hyperpolarized metabolic products. J Magn Reson. 2008;193:139–146. [PubMed: 18424203]
20. Gordon JW, Vigneron DB, Larson PEZ. Development of a symmetric echo planar imaging framework for clinical translation of rapid dynamic hyperpolarized 13C imaging. Magn Reson Med. 2017;77:826–832. [PubMed: 26898849]
21. Lau AZ, Chen AP, Ghugre NR, et al. Rapid multislice imaging of hyperpolarized 13C pyruvate and bicarbonate in the heart. Magn Reson Med. 2010;64:1323–1331. [PubMed: 20574989]
22. Shang H, Sukumar S, Morze C, et al. Spectrally selective three- dimensional dynamic balanced steady-state free precession for hyperpolarized C-13 metabolic imaging with spectrally selective radiofrequency pulses. Magn Reson Med. 2016;78:963–975. [PubMed: 27770458]
23. Månsson S, Petersson JS, Scheffler K. Fast metabolite mapping in the pig heart after injection of hyperpolarized 13C-pyruvate with low-flip angle balanced steady-state free precession imaging. Magn Reson Med. 2012;68:1894–1899. [PubMed: 22294528]
24. Xing Y, Reed GD, Pauly JM, Kerr AB, Larson PEZ. Optimal variable flip angle schemes for dynamic acquisition of exchanging hyperpolarized substrates. J Magn Reson. 2013;234:75–81. [PubMed: 23845910]
25. Maidens J, Gordon JW, Arcak M, Larson PEZ. Optimizing flip angles for metabolic rate estimation in hyperpolarized carbon-13 MRI. IEEE Trans Med Imaging. 2016;35:2403–2412. [PubMed: 27249825]
26. Schulte RF, Sperl JI, Weidl E, et al. Saturation-recovery metabolic-exchange rate imaging with hyperpolarized [1–13C] pyruvate using spectral-spatial excitation. Magn Reson Med. 2012;1209–1216. [PubMed: 22648928]
27. Larson P, eugene17uf, Gordon J, et al. LarsonLab/hyperpolarized-MRI-toolbox: Demo notebooks, new datasets 2020 10.5281/zenodo.3711662.

28. Gordon JW, Chen H-Y, Autry A, et al. Translation of Carbon-13 EPI for hyperpolarized MR molecular imaging of prostate and brain cancer patients. Magn Reson Med. 2019;81:2702–2709. [PubMed: 30375043]
29. Tang S, Milshteyn E, Reed G, et al. A regional bolus tracking and real-time B1 calibration method for hyperpolarized 13C MRI. Magn Reson Med. 2019;81:839–851. [PubMed: 30277268]
30. Jackson JI, Meyer CH, Nishimura DG, Macovski A. Selection of a convolution function for Fourier inversion using gridding (computerised tomography application). IEEE Trans Med Imaging. 1991;10:473–478. [PubMed: 18222850]
31. Pruessmann KP, Weiger M, Börnert P, Boesiger P. Advances in sensitivity encoding with arbitrary k-space trajectories. Magn Reson Med. 2001;46:638–651. [PubMed: 11590639]
32. Zhu Z, Zhu X, Ohliger MA, et al. Coil combination methods for multi-channel hyperpolarized 13C imaging data from human studies. J Magn Reson. 2019;301:73–79. [PubMed: 30851668]
33. Grist JT, McLean MA, Riemer F, et al. Quantifying normal human brain metabolism using hyperpolarized [1–13C]pyruvate and magnetic resonance imaging. NeuroImage. 2019;189:171–179. [PubMed: 30639333]
34. Lee CY, Soliman H, Geraghty BJ, et al. Lactate topography of the human brain using hyperpolarized 13C-MRI. NeuroImage. 2020;204:116202. [PubMed: 31557546]
35. Hu S, Larson PEZ, VanCriekinge M, et al. Rapid sequential injections of hyperpolarized [1–13C]pyruvate in vivo using a sub-kelvin, multi-sample DNP polarizer. Magn Reson Imaging. 2013;31:490–496. [PubMed: 23107275]
36. Josan S, Hurd R, Billingsley K, et al. Effects of isoflurane anesthesia on hyperpolarized 13C metabolic measurements in rat brain. Magn Reson Med. 2013;70:1117–1124. [PubMed: 23086864]
37. Niesporek SC, Hoffmann SH, Berger MC, et al. Partial volume correction for in vivo 23Na-MRI data of the human brain. NeuroImage. 2015;112:353–363. [PubMed: 25797831]
38. Torigian DA, Zaidi H, Kwee TC, et al. PET/MR imaging: Technical aspects and potential clinical applications. Radiology. 2013;267:26–44. [PubMed: 23525716]
39. Farkash G, Markovic S, Novakovic M, Frydman L. Enhanced hyperpolarized chemical shift imaging based on a priori segmented information. Magn Reson Med. 2019;81:3080–3093. [PubMed: 30652358]
40. Dwork N, Gordon JW, Tang S, O'Connor D, Larson PEZ. Dichromatic interpolation of magnetic resonance metabolic imagery. arXiv preprint arXiv:2003.05042. 2020.
41. Sotiropoulos SN, Jbabdi S, Andersson JL, Woolrich MW, Ugurbil K, Behrens TEJ. RubiX: Combining spatial resolutions for Bayesian inference of crossing fibers in diffusion MRI. IEEE Trans Med Imaging. 2013;32:969–982. [PubMed: 23362247]
42. Posse S, Otazo R, Dager SR, Alger J. MR spectroscopic imaging: Principles and recent advances. J Magn Reson Imaging. 2013;37:1301–1325. [PubMed: 23188775]
43. Evans NR, Tarkin JM, Buscombe JR, Markus HS, Rudd JHF, Warburton EA. PET imaging of the neurovascular interface in cerebrovascular disease. Nat Rev Neurol. 2017;13:676. [PubMed: 28984315]
44. Moses WW. Fundamental limits of spatial resolution in PET. Nucl Instrum Methods Phys Res, Sect A. 2011;648(Supplement 1):S236–S240. [PubMed: 21804677]
45. Maddahi J, Packard RRS. Cardiac PET perfusion tracers: Current status and future directions. Semin Nucl Med. 2014;44:333–343. [PubMed: 25234078]
46. Chen H-Y, Larson PEZ, Bok RA, et al. Assessing prostate cancer aggressiveness with hyperpolarized dual-agent 3D dynamic imaging of metabolism and perfusion. Can Res. 2017;77:3207–3216.
47. Qing K, Ruppert K, Jiang Y, et al. Regional mapping of gas uptake by blood and tissue in the human lung using hyperpolarized xenon-129 MRI. J Magn Reson Imaging. 2014;39:346–359. [PubMed: 23681559]
48. Reeder SB, Faranesh AZ, Boxerman JL, McVeigh ER. In vivo measurement of T*2 and field inhomogeneity maps in the human heart at 1.5 T. Magn Reson Med. 1998;39:988–998. [PubMed: 9621923]

49. Atalay MK, Poncelet BP, Kantor HL, Brady TJ, Weisskoff RM. Cardiac susceptibility artifacts arising from the heart-lung interface. Magn Reson Med. 2001;45:341–345. [PubMed: 11180442]

50. Geraghty BJ, Lau JYC, Chen AP, Cunningham CH. Dual-Echo EPI sequence for integrated distortion correction in 3D time-resolved hyperpolarized 13C MRI. Magn Reson Med. 2018;79:643–653. [PubMed: 28394085]

51. Miller JJ, Lau AZ, Tyler DJ. Susceptibility-induced distortion correction in hyperpolarized echo planar imaging. Magn Reson Med. 2018;79:2135–2141. [PubMed: 28722201]

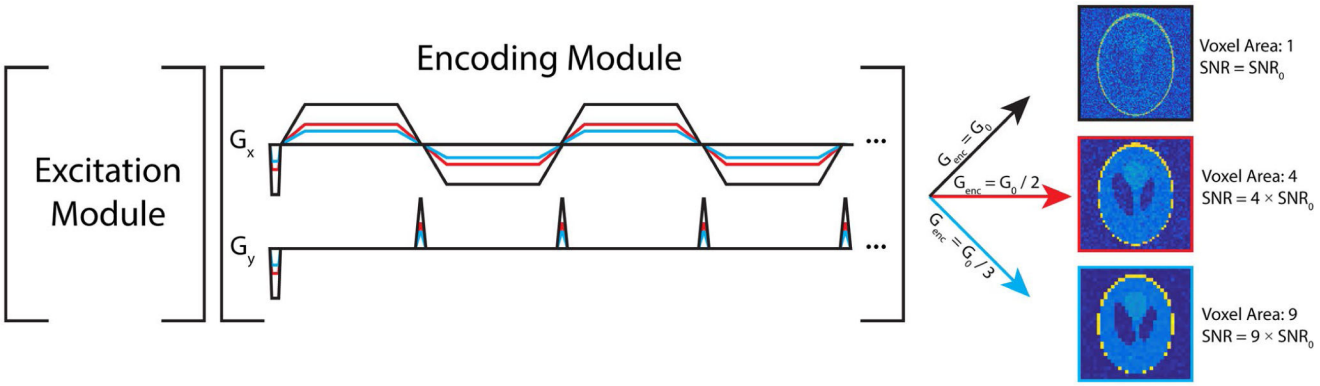

FIGURE 1.

Pulse sequence diagram for variable resolution imaging using an echoplanar readout. In this approach, a single-band SPSP RF pulse is used to independently excite each metabolite. The readout waveform, shown here as an echoplanar trajectory in the encoding module, can then be scaled to yield a voxel size based on the SNR for each metabolite

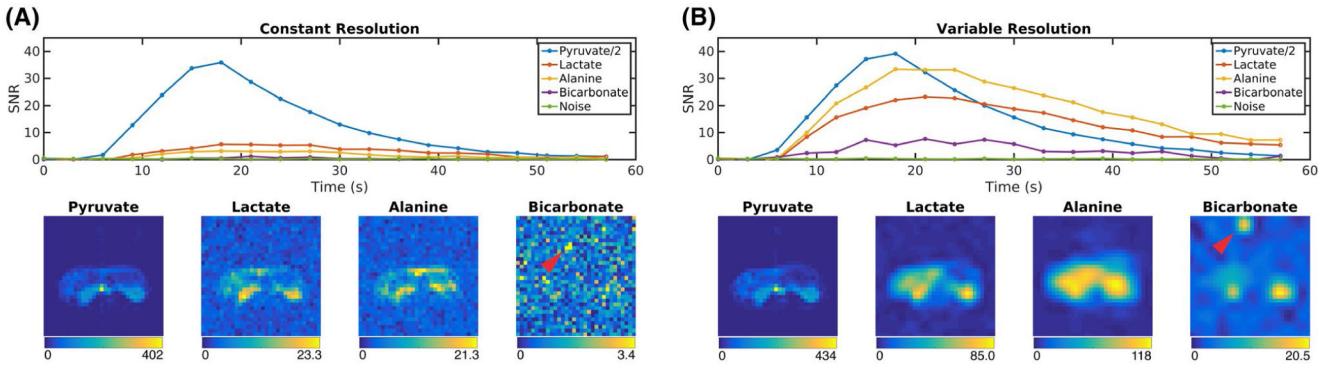

FIGURE 2.

Kinetics of hyperpolarized pyruvate renal metabolism from a single 20 mm slice in a healthy rat. The constant resolution data (A) were acquired at 2.5 × 2.5 mm^2 in-plane resolution for all metabolites, whereas for the variable resolution study (B) pyruvate was acquired at 2.5 × 2.5 mm^2, lactate was acquired at 5.0 × 5.0 mm^2, and bicarbonate and alanine at 7.5 × 7.5 mm^2. AUC maps (in SNR units) shown below the timecourse highlight the improvement provided by the variable resolution approach, especially for metabolites with low concentration such as bicarbonate. The red arrows indicate the location of the urea phantom, which was used for RF frequency and power calibration

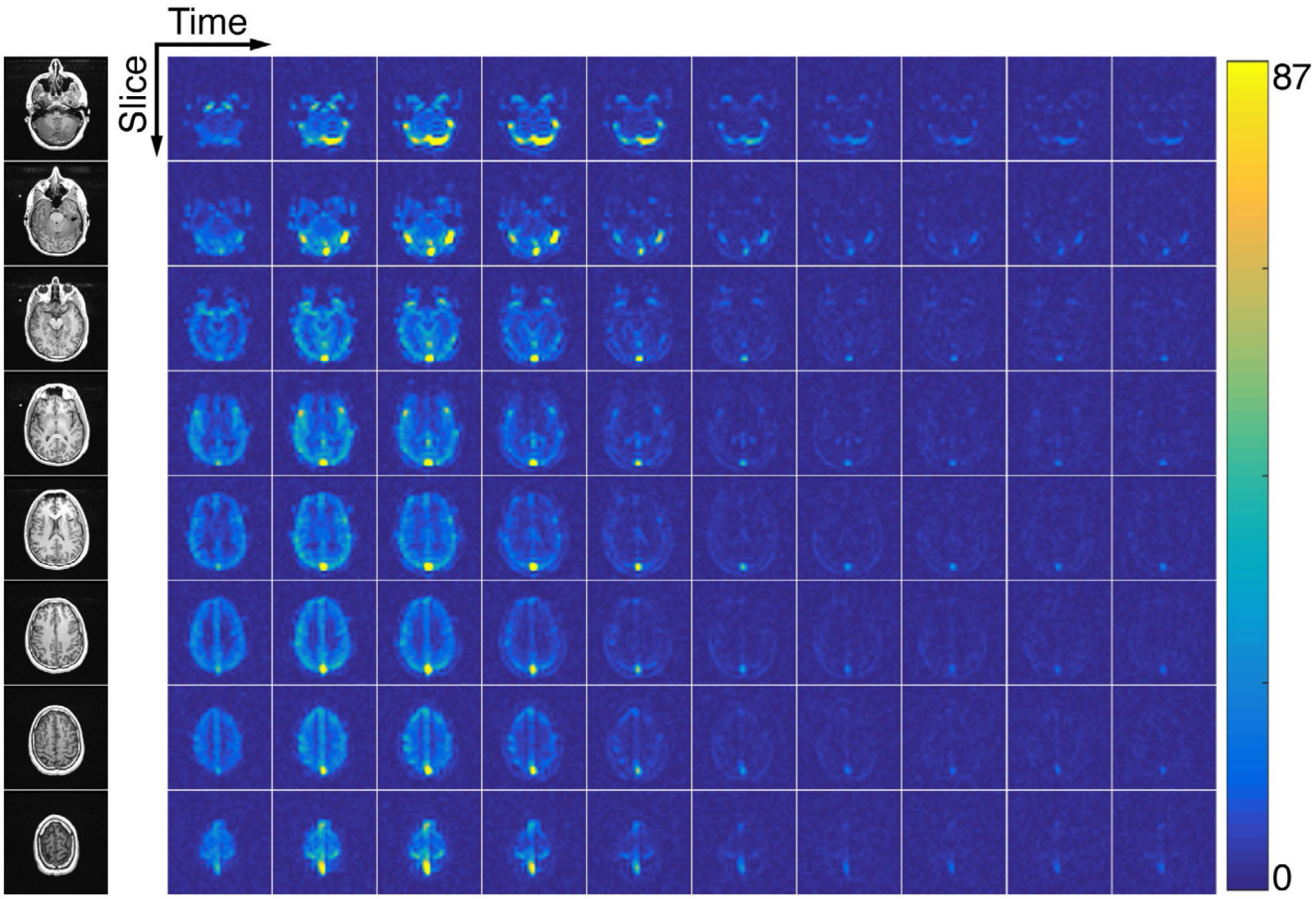

FIGURE 3.

The 4D dynamics of hyperpolarized [1-^{13}C]pyruvate in the healthy human brain. Eight 1.5-cm slices were acquired with a temporal resolution of 3 s. Data were acquired with an in-plane resolution of 0.75 × 0.75 cm^2 and are displayed in SNR units. Twenty total timeframes were acquired and the first 10 are shown here

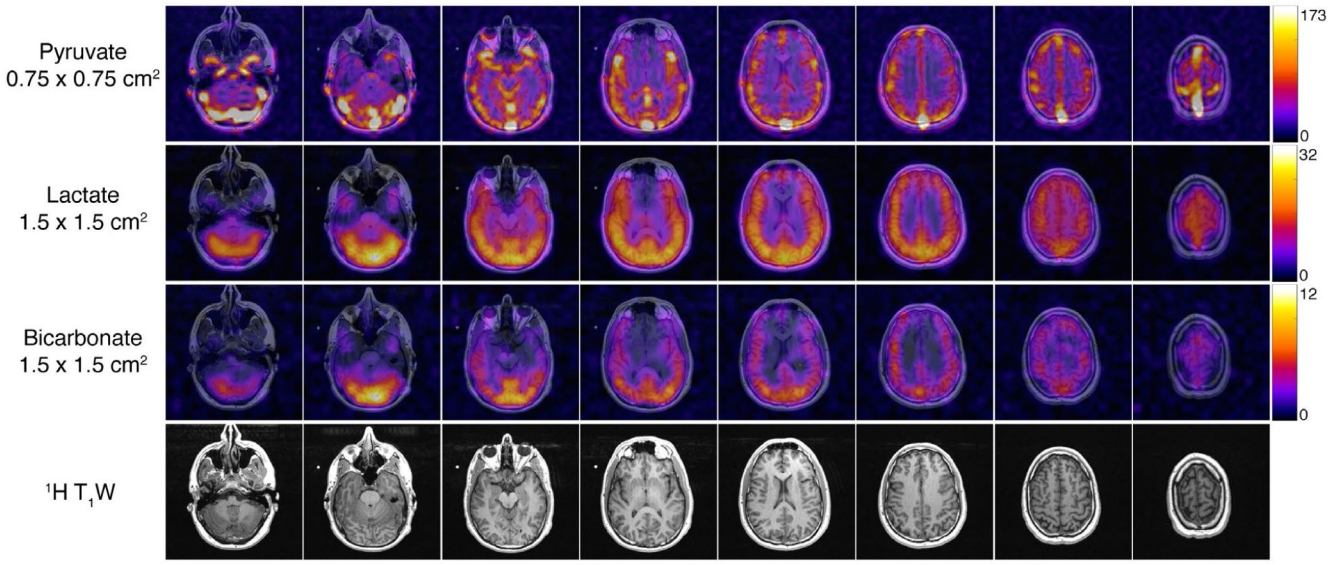

FIGURE 4.

AUC images from a healthy brain volunteer. The higher resolution pyruvate data set enabled improved visualization of neuro-vasculature while the lactate and bicarbonate images acquired at a coarser resolution retain sufficient SNR to visualize metabolism throughout the brain. Each metabolite map was zero-filled two-fold for display

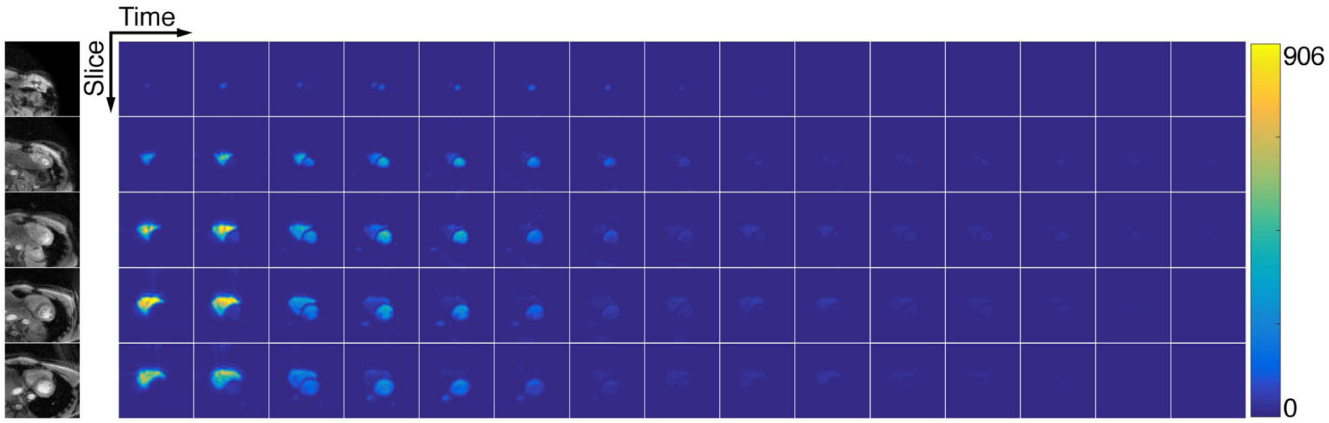

FIGURE 5.

The 4D dynamics of hyperpolarized [1-^{13}C]pyruvate in the healthy human heart. Five 2.1-cm slices were acquired with cardiac gating. Each metabolite volume was acquired within one heartbeat, yielding an effective temporal resolution of ~3.5 s. Data were acquired with an in-plane resolution of 0.6 × 0.6 cm^2 and are displayed in SNR units. Thirty total timeframes were acquired and the first 15 are shown here

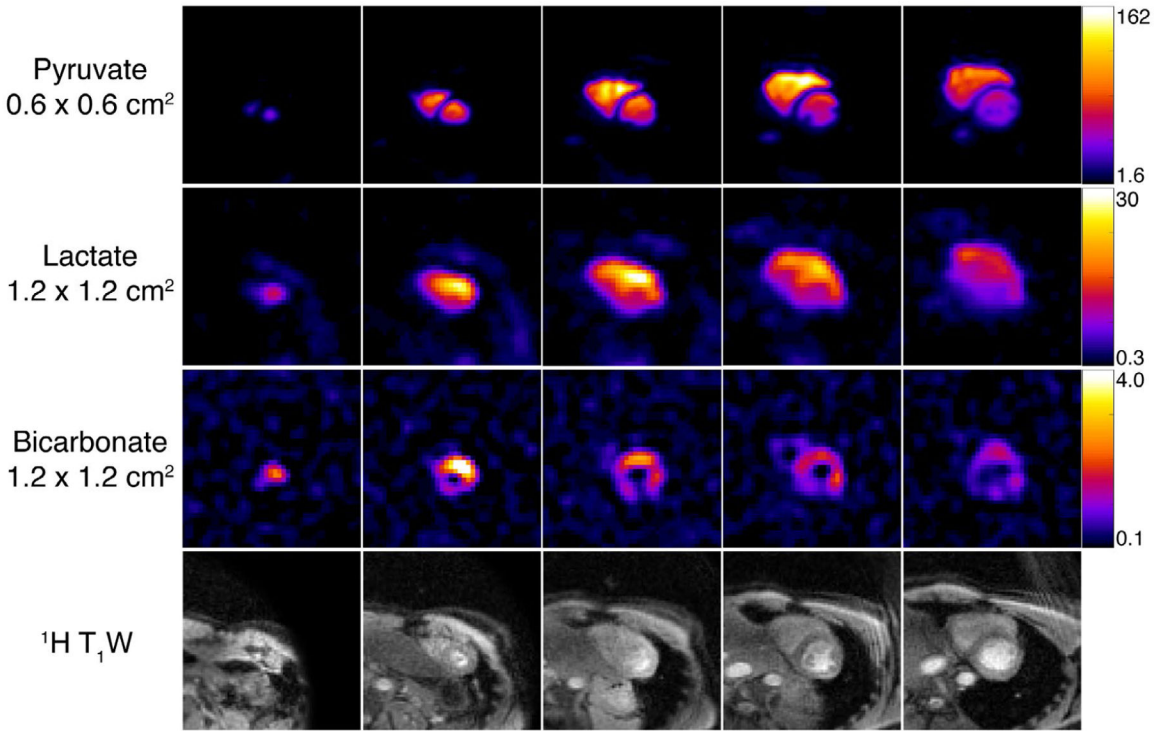

FIGURE 6.

AUC images from a healthy cardiac volunteer. The pyruvate data, acquired at finer resolution, provides improved contrast between the left and right ventricles and the myocardium and papillary muscles. The comparatively coarse resolution of lactate and bicarbonate data was better matched to the lower SNR of these metabolites and reveals relevant localization of bicarbonate primarily in the myocardium and lactate in both the myocardium and blood pool. Each metabolite map was zero-filled two-fold for display

TABLE 1

Peak SNR and AUC ratios (total metabolite signal divided by total pyruvate signal and normalized by voxel volume) for lactate, alanine, and bicarbonate in rat kidney experiments ($n = 4$) shown in Figure 2 and Supporting Information Figure S1

	Constant resolution		Variable resolution	
	Peak SNR	**AUC Ratio**	**Peak SNR**	**AUC Ratio**
Pyruvate	57.4 ± 21.0	N/A	55.3 ± 13.6	N/A
Lactate	4.3 ± 0.8*	0.143 ± 0.054	14.9 ± 2.3*	0.120 ± 0.034
Alanine	2.4 ± 1.0*	0.089 ± 0.042	20.9 ± 4.7*	0.070 ± 0.016
Bicarbonate	0.9 ± 0.3*	0.057 ± 0.031*	5.4 ± 2.4*	0.017 ± 0.010*
Noise ROI	N/A	0.054 ± 0.030	N/A	0.005 ± 0.002

Constant resolution data sets were acquired at 2.5 × 2.5 mm^2 for all metabolites. For variable resolution data sets, pyruvate was acquired at 2.5 × 2.5 mm^2 in-plane resolution, while lactate was acquired at 5.0 × 5.0 mm^2 and bicarbonate and alanine at 7.5 × 7.5 mm^2. For reference, a noise ROI shows the detectable limit for the constant resolution and variable-resolution at 7.5 × 7.5 mm^2. There was a significant difference (*$P < .05$) between the constant and variable resolution bicarbonate-to-pyruvate ratio, as well as the peak lactate, alanine, and bicarbonate SNR values.